Design, construction, and calibration of a three-axis, high-frequency magnetic probe (*B*-dot probe) as a diagnostic for exploding plasmas

E. T. Everson,[a] P. Pribyl, C. G. Constantin, A. Zylstra, D. Schaeffer, N. L. Kugland, and C. Niemann
Department of Physics and Astronomy, University of California, Los Angeles, Los Angeles, California 90095, USA

(Received 22 May 2009; accepted 19 September 2009; published online 18 November 2009)

A three-axis, 2.5 mm overall diameter differential magnetic probe (also known as *B*-dot probe) is discussed in detail from its design and construction to its calibration and use as diagnostic of fast transient effects in exploding plasmas. A design and construction method is presented as a means to reduce stray pickup, eliminate electrostatic pickup, reduce physical size, and increase magnetic signals while maintaining a high bandwidth. The probe's frequency response is measured in detail from 10 kHz to 50 MHz using the presented calibration method and compared to theory. The effect of the probe's self-induction as a first order correction in frequency, $O(\omega)$, on experimental signals and magnetic field calculations is discussed. The probe's viability as a diagnostic is demonstrated by measuring the magnetic field compression and diamagnetism of a sub-Alfvénic (~ 500 km/s, $M_A \sim 0.36$) flow created from the explosion of a high-density energetic laser plasma through a cooler, low-density, magnetized ambient plasma. © *2009 American Institute of Physics.*
[doi:10.1063/1.3246785]

I. INTRODUCTION

We have designed and constructed a small, three-axis, high-frequency magnetic (also known as *B*-dot) probe and supporting electronics to measure transient events in plasmas. Such phenomena include exploding plasmas,[1] magnetic shocks, rapidly expanding diamagnetic cavities in vacuum or surrounding plasma environments,[2–4] nonlinear Alfvén waves,[5] and many other nonlinear phenomena. Measuring these events can be difficult because one needs a probe that is sensitive to the three components of the field, can respond quicker than the time scales of interest, has a size smaller than the Larmor radius, and is sufficiently sensitive to measure weak (a few Gauss) magnetic fields.

In the laboratory setting it is extremely difficult to meet these physical restrictions. In our laser-plasma experiments, discussed in further detail in Sec. IV B, a magnetized shock is driven through a helium plasma with initial density of $\sim 2\times 10^{12}$ cm^{-3}, electron temperature of ~ 6 eV, ion temperature of ~ 1 eV, and background field of 1800 G. Under these conditions the electron Larmor radius is ~ 36 μm and the ion Larmor radius is ~ 1 mm. Magnetic probes used for experiments on plasma thrusters[6–8] or basic plasma science experiments[1,5,9] are typically larger and are not used at frequencies above a few kilohertz. Our probe is designed with a 1.25 mm radius (2.5 mm outer diameter) tip, which approaches the scale of the ion Larmor radius while maintaining a bandwidth of 50 MHz.

Important probe characteristics, such as sensitivity and response, are determined by the probe's internal resistance, internal capacitance, self-inductance, load resistance, and noise levels. In the subsequent sections these parameters will be discussed in detail as we describe the design, construction, calibration, and application of the three-axis, high-frequency magnetic probe. The design and construction section will describe the overall layout of the device, the materials used, and why this approach was taken. Section III describes the probe theory and the implemented calibration method. In Sec. IV, the probe parameters determined by the calibration are applied to experimental data.

II. PROBE DESIGN AND CONSTRUCTION

Our design follows the classical magnetic pickup coil design,[6–14] which utilizes Faraday's law to detect magnetic field fluctuations. In this design (Fig. 1) we can think of the probe as having three key elements: (1) the probe tip, (2) the probe shaft and enclosure, and (3) the differential amplifier. The probe tip is the heart of the device and has three sets of wire loops sensitive to the three components of the magnetic field at a given point. The probe shaft and enclosure is designed to transmit the signals to the differential amplifier, protect the sensory elements from plasma saturation current, and reduce stray pickup. Finally, a high-frequency differential amplifier mitigates much of the electrostatic pickup from the plasma.

The probe tip consists of a 2×2 mm cylindrical Vespel® SP-1 core machined down to create a 1×1 mm cube at the center with feet at each corner. Vespel® is used because of its high thermal capabilities, machinability, and relative magnetic permeability near unity at high frequencies. Using the troughs created by the feet on the core, we wind a twisted pair of no. 43 polyimide insulated copper wire around the core for five times. This creates a differential pair of five turn loops, loop 1 and loop 2, or ten total turns

[a]Electronic mail: eeverson@ucla.edu.

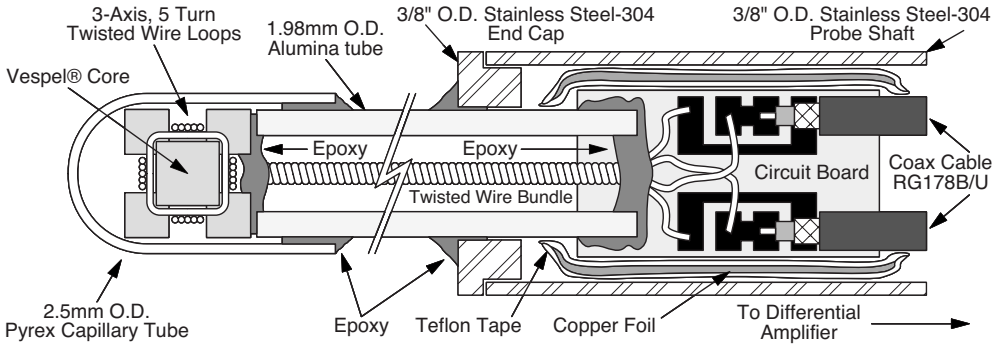

FIG. 1. Cross-sectional view of the probe.

along each axis. As a result, magnetic fields induce equal but opposite voltages in loop 1 and loop 2, while induced electrostatic voltages have the same polarity. Thus, when subtracting the loop 1 and loop 2 signals, the electrostatic components are subtracted out, while the magnetic components are doubled.

The 12 leads, four per axis and two per loop, coming off the core are carefully twisted into a tight bundle to reduce any stray pickup along their length. The twisted bundle of leads is then passed through a 20 cm long alumina tube with a 2.0 mm outer diameter and 1.2 mm inner diameter. To prevent the twisted bundle from unraveling, the core is epoxied to one end of the alumina tube and the wires to the other end with Loctite® Hysol® 1C™ resin. The alumina tube behaves as a good insulator to protect the leads from the surrounding plasma. A 2.5 mm outer diameter quartz capillary tube is also epoxied to the alumina tube to protect the probe tip.

Since our stainless steel probe shaft is 1.4 m long, it is unreasonable to have the twisted pair of wire leads run the length of the shaft for two key reasons. First, the leads easily break, and second, it is difficult to keep the leads from forming closed loops and causing stray pickup. Instead, the 12 leads are connected to six 50 Ω coax cables (RG178B/U). This connection is made by epoxying a small circuit board to the end of the alumina tube (Fig. 1). The circuit board contains a contact pattern for easy soldering. With the six coax cables soldered to the circuit board, each lead and its corresponding pair, e.g., the leads for loop 1 in Fig. 2, are cut to length and soldered to one of the six cables. Then the loop 2 leads are soldered to another coax cable in the reverse direction of loop 1. This process is repeated for each axis and connects the loops in an arrangement that forms the differential pair.

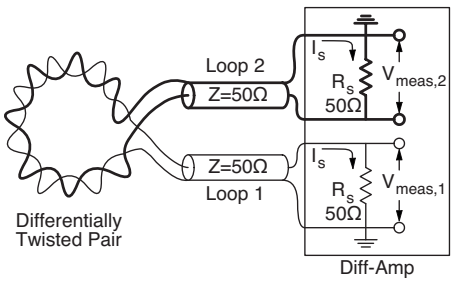

FIG. 2. Circuit schematic of a differentially wound pair of loops for one axis of the probe.

If the connections to the coax cables are not properly shielded and isolated from the plasma, then the connections can pickup plasma current and/or magnetic field fluctuations that contaminate the desired signals. To isolate the circuit board and reduce pickup, the board is wrapped in two layers of Teflon® tape with a thin 50 μm copper foil sandwiched between each layer (see Fig. 1). Finally, the bundle is inserted into the stainless steel shaft and capped off, isolating it from the plasma.

The other end of the probe shaft is sealed off with a vacuum tight KF-40 Delrin cap containing six LEMO® connector feedthroughs. Each coax cable is connected to one LEMO® connector. A Delrin cap is used to keep the probe internals isolated from the probe shaft and plasma. Each axis pair is then terminated with a 50 Ω load at the input of the differential amplifier (see Fig. 2).

A high-frequency (~100 MHz), custom-built differential amplifier is used to mitigate the electrostatic pickup created when a probe is inserted into a plasma. When a probe is placed in a plasma, there is a potential difference between the probe and the plasma, which shows up as a capacitive effect on the probe. This capacitive effect is substantially identical on both loop 1 and loop 2, which shows up as a common mode potential $V_{\text{electrostatic}}$. Since the electrostatic potential is identical on both loops, the differential amplifier subtracts out the common induced voltage to create the final signal $V_{\text{meas}}(t)$.

III. CALIBRATION TECHNIQUE

A common calibration method is to create a known magnetic field and compare it to the resulting magnetic probe signal.[6,12–17] There are numerous ways to generate the magnetic field (e.g., a Helmholtz coil, a loop coil, a straight piece of wire, etc.), but each field generator has its own limitations. Some of these limitations include bandwidth, uniformity of the generated magnetic field, required driver power, and stray capacitances.[16,17]

Utilizing the mentioned magnetic field generators, the magnetic probe response can be characterized. There are several ways to characterize the response of the probe; for example, in Ref. 17 the probe's impedance is measured, while

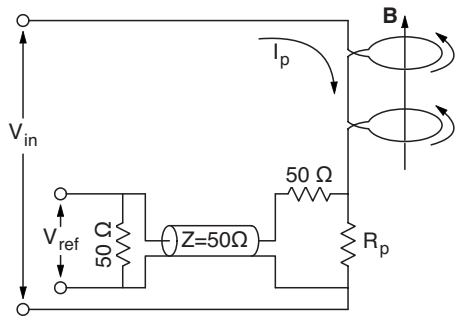

FIG. 3. The Helmholtz circuit schematic used for generating a known frequency varying magnetic field for the calibration.

in Refs. 15 and 16, the scattering parameters of the probe and magnetic field generators are measured. In the following technique the frequency response is measured by comparing the output of the probe V_{meas} to the current through (or magnetic field of) the magnetic field generator as measured over a small resistor R_P (see Fig. 3).

To implement this technique, a magnetic field generator is driven with a known frequency swept signal from a network analyzer. For low frequencies, 10–500 kHz, we use a Helmholtz coil to produce a test magnetic field. At higher frequencies the inductance of the Helmholtz coil limits the current and, thus, reduces the sensitivity of this method to below the noise level. To reach higher frequencies, 10 kHz–50 MHz, we replace the Helmholtz coil (shown in Fig. 3) with a short piece of wire and a 50 Ω resistor. The 50 Ω resistor, which is required for impedance matching, is shielded inside a copper tube to mitigate any radiation that may cause electromagnetic interference.

A. Calibration theory

As described in the previous section, the pickup loops of the probe consist of a pair of twisted wires turned five times around a Vespel® SP-1 plastic core. As shown in Fig. 2, the only difference between the two sets of loops, loop 1 and loop 2, is the location of ground. Taking a closer look at the loop 1 circuit[15] (Fig. 4) and assuming that the current through loop 1 is equal to the current through loop 2, one can write out the circuit equation

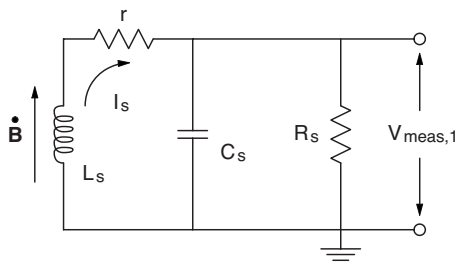

FIG. 4. Circuit schematic for one loop (loop 1) of a differentially wound pair used in the probe tip as a magnetic field pickup.

$$an\frac{d}{dt}B(t)=\left(1+\frac{r}{R_s}\right)V_{\mathrm{meas},1}(t)+\left(\frac{L_s+M}{R_s}+rC_s\right)\frac{d}{dt}V_{\mathrm{meas},1}(t)+(L_s+M)C_s\frac{d^2}{dt^2}V_{\mathrm{meas},1}(t), \quad (1)$$

where a is the area of a single turn, n is the number of turns in a loop, r is the internal resistance of the loop, R_s is the load resistance on the loop, L_s is the self-inductance of the loop, M is the mutual-inductance between the two loops, and C_s is the internal capacitance of the loop. The magnetic field $B(t)$ created by either the Helmholtz coil or wire acts as a voltage source for the circuit. In the case of the Helmholtz coil, this term is just the mutual-inductance between the Helmholtz coil and the loop.

Taking the Fourier transform of Eq. (1) and collecting terms, one can determine an expression between $V_{\mathrm{meas},1}(\omega)$ and $B(\omega)$ in frequency space,

$$\frac{V_{\mathrm{meas},1}(\omega)}{B(\omega)}=an\frac{\omega^2(\tau_s+rC_s)+i\omega[(1+\rho_s)-R_s\tau_sC_s\omega^2]}{[(1+\rho_s)-R_s\tau_sC_s\omega^2]^2+\omega^2(\tau_s+rC_s)^2}, \quad (2)$$

where $\rho_s=r/R_s$ and $\tau_s=(L_s+M)/R_s$. For large ω the real part of Eq. (2) falls off like $1/\omega^2$, and the imaginary part falls off like $1/\omega$, causing $V_{\mathrm{meas},1}(\omega)\to 0$ as $\omega\to\infty$. Since the capacitor behaves like a short at high frequencies, it puts a limit on the probes operational frequency range. Assuming $\rho_s \ll 1$ and $\omega C_s R_s \ll 1$, then Eq. (2) can be simplified to

$$\frac{V_{\mathrm{meas},1}(\omega)}{B(\omega)}=an\frac{\omega}{1+(\omega\tau_s)^2}[\omega\tau_s+i], \quad (3)$$

for which the frequency range is $0<\omega\ll 1/R_sC_s$.

Since the circuits for loop 1 and loop 2 are identical except for the placement of ground, we can say that $V_{\mathrm{meas},1}(t)=-V_{\mathrm{meas},2}(t)$. Thus, the resulting expression after the differential amplifier is

$$\frac{V_{\mathrm{meas}}(\omega)}{B(\omega)}=2g\frac{V_{\mathrm{meas},1}(\omega)}{B(\omega)}=aNg\frac{\omega}{1+(\omega\tau_s)^2}[\omega\tau_s+i], \quad (4)$$

where N is the total number of turns between the two loops and g is the gain of the differential amplifier. At low frequencies, $\omega\tau_s \ll 1$, Eq. (4) reverts back to the well-known B-dot signal in which the probe's signal V_{meas} is proportional to the first time derivative of the magnetic field. At higher frequencies, $1\ll\omega\tau_s\ll\tau_s/R_sC_s$, all frequency dependence in Eq. (4) drops out. As a result, in this frequency range the probe's signal is directly proportional to the magnetic field.

B. Calibration method

The calibration method utilized here uses known time varying magnetic fields to determine key characteristics of the probe, such as area per turn and τ_s. To calculate these parameters the calibration setup utilizes the four components in Fig. 5: (1) an Agilent/HP E5100 10 kHz–180 MHz network analyzer, (2) a magnetic field generator, (3) a magnetic probe, and (4) a differential amplifier. The magnetic field

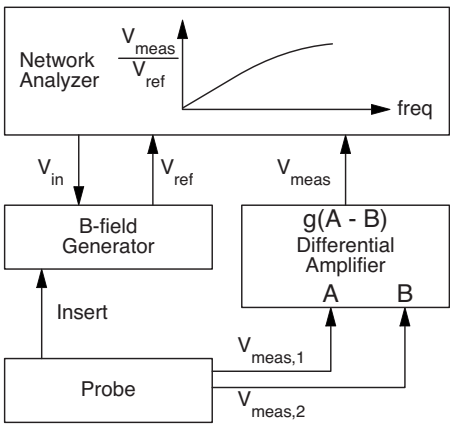

FIG. 5. Block diagram of the calibration setup used to measure the frequency response of the probe.

generator is either a Helmholtz coil (Fig. 3) or a straight wire. For both circuits the network analyzer supplies the necessary voltage $V_{\text{in}}(t)$ to create the time varying fields and measures the reference voltage $V_{\text{ref}}(t)$ across R_p to compare to the probe's response $V_{\text{meas}}(t)$. When positioned correctly the magnetic field will only induce a voltage along one of the probe axes. The network analyzer then compares $V_{\text{ref}}(t)$ and $V_{\text{meas}}(t)$ and generates the real and imaginary parts of $V_{\text{meas}}(\omega)/V_{\text{ref}}(\omega)$, which correspond to Eq. (4). There are cable length differences between the probe and magnetic field generator circuits, so we have to introduce an electrical time delay τ into Eq. (4) to get

$$\frac{V_{\text{meas}}(\omega)}{B(\omega)} = aNg\frac{\omega}{1+(\omega\tau_s)^2}[\omega\tau_s + i]e^{i\omega\tau}$$

$$= aNg\frac{\omega}{1+(\omega\tau_s)^2}\{[\omega\tau_s\cos(\omega\tau) - \sin(\omega\tau)]$$

$$+ i[\omega\tau_s\sin(\omega\tau) + \cos(\omega\tau)]\}. \quad (5)$$

For low frequencies (10–500 kHz), we utilize the Helmholtz circuit to create a calibration magnetic field. At the center of the Helmholtz coil, the field is given by

$$B(\omega) = \left(\frac{4}{5}\right)^{3/2}\frac{\mu_o}{rR_p}[2V_{\text{ref}}(\omega)], \quad (6)$$

where r is the radius of the Helmholtz coil. The relative permeability μ_r for the Vespel® core is close to unity. Combining Eq. (6) with Eq. (5) and expanding to lowest order in $|\omega\tau_s| \ll 1$ and $|\omega\tau| \ll 1$, we get

$$\frac{V_{\text{meas}}(\omega)}{V_{\text{ref}}(\omega)} = aNg\left(\frac{16}{5^{3/2}}\right)\frac{\mu_o}{rR_p}[(\tau_s - \tau)\omega^2 + i\omega]. \quad (7)$$

This form is a good approximation for our frequency range, as seen in Fig. 6. The valid frequency range for this approximation varies depending on the probe size, design, and construction. The real component in Eq. (7) yields very little useful information, but the area per turn can be directly calculated from the slope of the imaginary component. For this probe the area per turn a in the x-direction is 2.002 mm^2, y-direction is 1.638 mm^2, and z-direction is 1.740 mm^2.

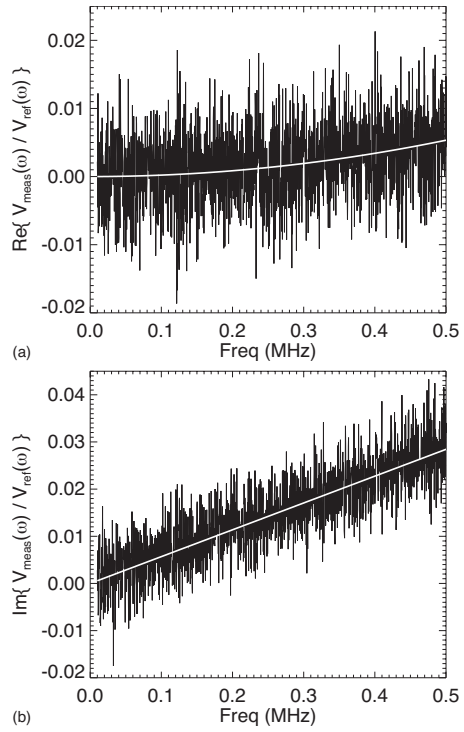

FIG. 6. The probe's z-axis frequency response from 10 to 500 kHz as determined from the calibration with the Helmholtz coil. The theoretical fit (white), as determined by Eq. (7), is plotted against the Helmholtz calibration data (solid) for the (a) real and (b) imaginary parts.

For higher frequencies (10 kHz–50 MHz), we can use the wire circuit and its field to measure τ_s and the electrical time delay τ. In this case the field is given by

$$B(\omega) = \frac{\alpha\mu_o}{2\pi rR_p}[2V_{\text{ref}}(\omega)], \quad (8)$$

where r is the distance from the wire to the probe tip and α is a geometry factor related to the length of the wire and the current return path. Combining Eq. (8) with Eq. (5), we obtain a full expression,

$$\frac{V_{\text{meas}}(\omega)}{V_{\text{ref}}(\omega)} = \frac{aNg\alpha\mu_o}{\pi rR_p}\frac{\omega}{1+(\omega\tau_s)^2}\{[\omega\tau_s\cos(\omega\tau) - \sin(\omega\tau)]$$

$$+ i[\omega\tau_s\sin(\omega\tau) + \cos(\omega\tau)]\}, \quad (9)$$

which accurately represents the probe's response up to 40 MHz (see Fig. 7). At about 40 MHz the calibration measurement and theory begin to deviate. The difference is likely due to rf pickup along the probe shaft and coax cables from the magnetic field source. Using the calibration fit, this probe yields a τ_s and τ of 5.343 and −46.35 ns for the x-axis, 4.770 and −46.18 ns for the y-axis, and 4.169 and −46.78 ns for the z-axis.

In this frequency range the capacitive effects for this probe are negligible, but the self-inductance effects are not. This is not the case for all probes, that is, probes with larger areas, larger wires, and more turns can easily bring the self-resonance down to a few megahertz. The easiest way to determine what effects are present is to look at the magnitude of the frequency response. If both the self-inductance and capacitance effects are negligible, then the magnitude will

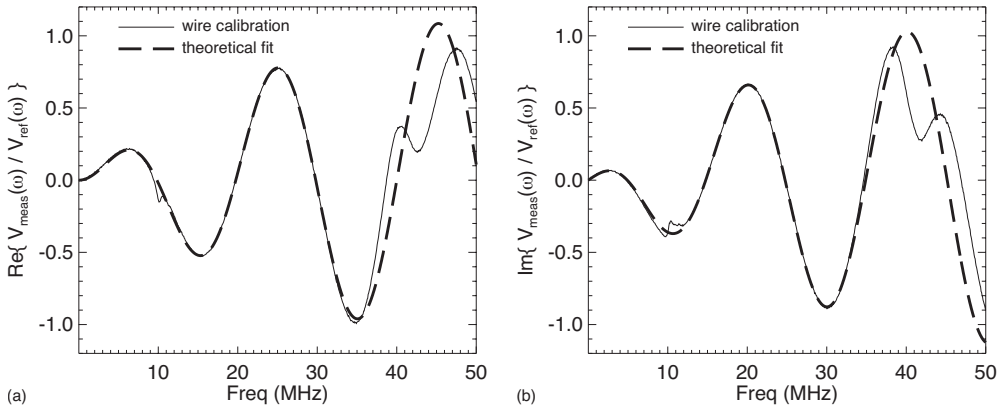

FIG. 7. The probe's z-axis frequency response form 10 kHz to 50 MHz as determined from the calibration with the wire. The theoretical fit (dashed), as determined by Eq. (9), is plotted against the wire calibration data (solid) for the (a) real and (b) imaginary parts.

increase linearly in frequency. If only the capacitance in negligible, then the magnitude will plateau as $\omega \to \infty$. If neither is negligible, then after the magnitude peaks, it will roll off and fall to zero as $1/\omega^2$.

IV. CALCULATING MAGNETIC FIELDS FROM PROBE SIGNALS

There are several ways to extrapolate a magnetic field $B(t)$ from a probe signal $V_{\text{meas}}(t)$. First, we could discretely integrate the signal according to the model given by the circuit equation

$$aNg\frac{d}{dt}B(t) = \left[1 + \tau_s\frac{d}{dt}\right]V_{\text{meas}}(t), \tag{10}$$

where a and τ_s are the parameters determined in the calibration. Second, we could take the discrete Fourier transform of $V_{\text{meas}}(t)$ using the fast Fourier transform (FFT) algorithm, apply Eq. (4), and apply the inverse-FFT to determine $B(t)$. Third, we could use a hybrid method constructed from the two previously mentioned methods to give Eq. (12). The FFT method has a hidden trap in its application. When converting $V_{\text{meas}}(\omega)$ to $B(\omega)$, a singularity is introduced at $\omega = 0$. As a result, the one-to-one correspondence between $V_{\text{meas}}(\omega)$ and $B(\omega)$ is destroyed. The destruction of the one-to-one correspondence occurs when the $\omega=0$ component of $V_{\text{meas}}(\omega)$ is nonzero. This situation may arise for several physical and nonphysical reasons: a dc offset in the signal, a slow variation in the background field that occurs on a time scale longer than the measurement time period, noise, or numerical errors. Regardless of the reason, a nonzero $\omega=0$ component [i.e., $V_{\text{meas}}(\omega=0) \neq 0$] will cause the breakdown. This is easily seen by first assuming $V_{\text{meas}}(t)$ is a constant V_m, i.e., $V_{\text{meas}}(\omega) = V_m\delta(\omega)$. According to Eq. (10), $B(t)$ then becomes

$$B(t) = B_o + \frac{V_m}{aNg}t. \tag{11}$$

Since $B(t)$ now has a linear term in time, $B(\omega)$ has many nonzero components other than the $\omega=0$ component. As a result, the $\omega=0$ term of $V_{\text{meas}}(\omega)$ is spread out over many frequencies in $B(\omega)$. For this reason we opt to use either the integration method or hybrid method.

The hybrid method follows along the same lines as the FFT method, but avoids the $\omega=0$ singularity and maintains the one-to-one correspondence. In this method the FFT is only applied to the right-hand-side of Eq. (10), giving

$$aNg\frac{d}{dt}B(t) = \text{FFT}^{-1}[(1 + i\omega\tau_s)V_{\text{meas}}(\omega)]. \tag{12}$$

That is, the signal $V_{\text{meas}}(t)$ is processed by taking the FFT, multiplying by $1+i\omega\tau_s$, and taking the inverse-FFT. The magnetic field is then determined by discretely integrating the processed signal according to Eq. (12).

This hybrid method and the integration method [Eq. (10)] are essentially identical. The only significant difference between the two methods is the number of computations needed, N computations for the integration method and $N + 2N\log(N)$ computations for the hybrid method. Since the integration method requires fewer computations, we opt to use it over the hybrid method. However, the hybrid method is much more illuminating in how the first order $O(\omega)$ correction term, or self-inductance term, affects the magnetic field calculation. For low frequency signals ($\omega\tau_s \ll 1$), Eq. (12) shows that $V_{\text{meas}}(\omega)$ remains relatively unchanged and the self-inductance term is negligible. At high frequencies ($\omega\tau_s \gtrsim 1$), the signal $V_{\text{meas}}(\omega)$ acquires a phase shift of $\tan^{-1}(\omega\tau_s)$ and a signal gain of $\sqrt{1+(\omega\tau_s)^2}$. This is due to the fact that the induced emf increases with the frequency of the magnetic field, which causes the self-inductance to act more strongly to reduce the emf. This is apparent in Eq. (10) by just moving the self-induction term to the left-hand-side and grouping it with the induced emf term. Thus, at high enough frequencies ($\omega\tau_s \gtrsim 1$), the self-induction of the probe reduces the induced emf enough that it needs to be corrected for. The effects and implications of this correction will be discussed in further detail in Sec. IV B.

A. Test field

To ensure that the probe and calibration method works properly, a test field is created that emulates a large amplitude Alfvén wave ($\sim$100 G and 50 kHz) observed in experiments.[18] The test field is generated from a switchable RLC circuit (Fig. 8). While the MOSFET is off, the 100 nF capacitor ($\pm$10 nF) is charged to 502 ± 3 V. When the

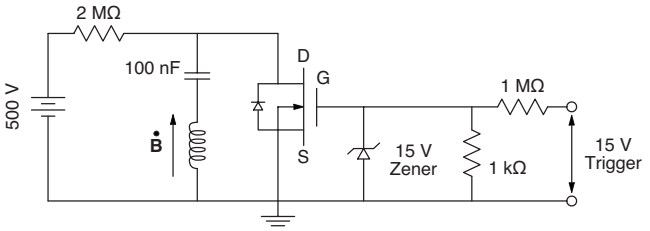

FIG. 8. The circuit schematic used to generate the damped-harmonic magnetic field for testing the probe's construction and calibration.

MOSFET is turned on, it causes the circuit to switch into RLC mode. In this mode the resistance $(0.72 \pm 0.05\ \Omega)$ is a combination of the effective resistance of the wire and MOSFET. The inductor is made from ten turns of 0.75 mm diameter wire wound in a 21 mm radius circle. The self-inductance of an inductor of this type can be approximated by

$$L \simeq \mu_o N^2 R_o \left[\ln\left(\frac{8R_o}{a}\right) - 2 \right], \tag{13}$$

where μ_o is the permeability constant, N is the number of turns, R_o is the radius of the inductor, and a is the radius of the wire. The inductor has an approximate self-inductance of $10.8 \pm 0.4\ \mu$H.

Assuming that all the electrostatic energy initially stored in the capacitor, $CV^2/2$, is completely converted into magnetic energy in the inductor, $LI^2/2$, the maximum current through the inductor is approximated as 48.2 ± 2.6 A. The magnetic field at the center of the inductor is given by

$$B(r=0) = \frac{\mu_o N}{2R_o} I. \tag{14}$$

Thus, the maximum possible magnetic field is 144 ± 8 G, which should be slightly larger than the largest measured magnetic field. The decay constant for the signal is given by $R/2L$, $(3.32 \pm 0.26) \times 10^4\ \text{s}^{-1}$. This decay constant in combination with the maximum possible field gives an accurate decay envelope for the test field [see Fig. 9(a)].

As a secondary measurement, a high current toroid inductor, current transformer, is used to measure the current flowing through the coil and, hence, the magnetic field. Both the current transformer and probe data are recorded on a 14-bit, 100 MHz data acquisition (DAQ) system. Applying the test field to the x-axis of the probe and calculating the magnetic field according to the integration method mentioned above, Fig. 9(a) shows that the current transformer measurement and probe measurement correlate well early in time and are bounded by the theoretical decay envelope well within the uncertainty. Later in time, $>80\ \mu$s, the probe measurement begins to deviate from the current transformer measurement and drift away from the zero axis. This drift is due to the discrete integration used to calculate the magnetic field, which is tied into the aliasing of the original signal. As with any discrete integration, this drift error is highly dependent on how finely or coarsely the data are acquired relative to the signal's maximum frequency. Taking the same test field and acquiring it on an 8-bit, 25 MHz oscilloscope, opposed to the 14-bit, 100 MHz digitizer, one can see in Fig. 9(b) that the drift in the magnetic field is much more severe (by a factor of ten).

Regardless of this integration error, the test field and secondary current transformer measurements show that the probe theory and calibration method are accurate. However, when analyzing signals one does need to be aware of how the signal is digitized and the resulting integration error incurred when calculating the magnetic field.

B. Application to exploding plasmas

This probe was used to investigate the dynamics of exploding laser-produced plasmas in the large plasma device (LAPD).[19] In this experiment a laser-produced blow-off plasma is used to shock a colder, low-density magnetized background plasma. The blow-off plasma is generated by irradiating a graphite target with a 25 J, 5 ns full width at half maximum (FWHM) laser pulse operating at a wavelength of 1064 nm. The graphite target is embedded in the magnetized background plasma column created by the LAPD, as shown in Fig. 10. The LAPD produces a He-plasma column that is 18 m long with a 75 cm diameter and a 10 ms plasma pulse duration.[19] The plasma column is created with a density of

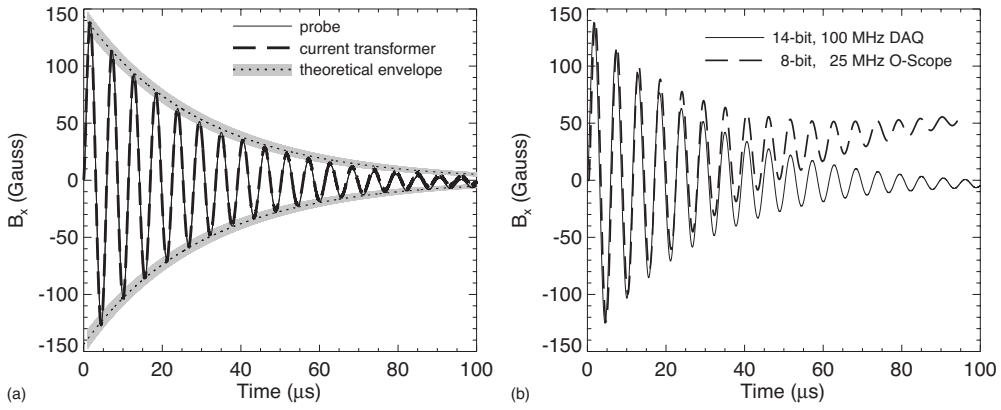

FIG. 9. Comparison of magnetic field measurements of the field generated from the circuit in Fig. 8. In plot (a) it is shown that the probe measurement (solid) is in good agreement with the field measure by the current transformer (dashed) and the theoretical decay envelope (shaded/dotted). In plot (b) the probe measurement taken on a 14-bit, 100 MHz DAQ system (solid) is compared to the one taken on an 8-bit, 25 MHz oscilloscope (O-scope) (dashed) and shown that the drift caused by integration is more sever with a slower sample rate.

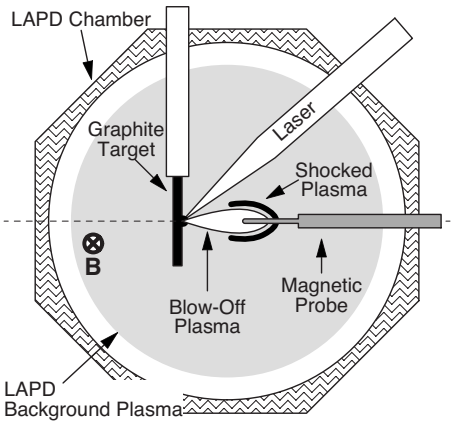

FIG. 10. End-on view of the experimental setup on the LAPD. The laser blow-off from the graphite target expands across the magnetic field lines. The magnetic probe comes in normal to the target face and perpendicular to the magnetic field.

$\sim 2\times 10^{12}$ cm^{-3}, electron temperature of ~ 6 eV, and ion temperature of ~ 1 eV. Additionally, the LAPD is capable of creating an axial dc magnetic field between 300 and 1800 G running the length of the chamber.

With the laser beam incident at about a 36° angle from the target normal, the blow-off plasma is allowed to explode across the magnetic field lines and shock the background plasma (Fig. 10). The magnetic probe is positioned directly in front of the target on a one-dimensional motorized probe drive that can be translated horizontally in and out. By repositioning the probe with each new laser shot, we are able to measure the evolution of the magnetic perturbations resulting from the interaction between the laser-produced plasma and the background LAPD plasma, which will be described in detail elsewhere. In the past, similar measurements used to study shear Alfvén waves were successfully performed in the LAPD (Ref. 20) with larger probes and at lower laser energies.

With the probe positioned 4.0 cm from the target (9.0 cm from chamber center) and the background field at 1800 G, the probe signal $V_{\text{meas}}(t)$ along the z-axis is acquired (Fig. 11). The leading edge of the signal expands away from the target at about 500 km/s with an Alfvén–Mach number M_A of about 0.36. In the first 300 ns after the laser fires, the signal displays a trace that is indicative of a diamagnetic bubble

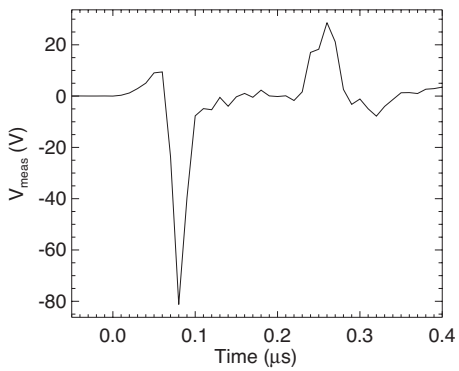

FIG. 11. A typical z-axis magnetic probe signal at 4 cm from the target and at a 1800 G background field.

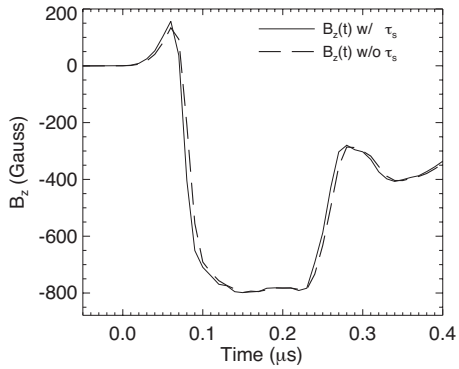

FIG. 12. Comparison of the z-component magnetic field calculations (including and not including the τ_s correction) at 4 cm from the target.

formation and propagation.[21,22] The first two spikes show the rise and drop in the leading edge of the bubble, which are then followed by a plateau. The third spike around 300 ns indicates the collapse of the bubble.

The signal in Fig. 11 was taken on a 14-bit, 100 MHz DAQ system, so the largest resolvable frequency is the Nyquist frequency, 50 MHz. Using a τ_s of 4.169 ns, as determined in the calibration, a signal at 50 MHz would have a $\omega\tau_s$ of 1.31. This leads us to believe that the self-induction term will be significant for the higher end of our frequency range, $\gtrsim 38$ MHz, but negligible for the lower frequencies.

Applying the magnetic field calculation to the trace in Fig. 11 we can see the effect of the self-induction term on the magnetic field (see Fig. 12). The first apparent observation is a steepening of the rising and trailing edges; however, for this signal it is not a significant change, less than a fraction of a percent. More important is the increase in the peak magnitudes. The first peak in the magnetic field has about a 17% increase in magnitude, reaching ~ 157 G above the background when the self-induction correction term is included. This is a modest correction because the frequency of the peak is well below 50 MHz. The first peak in Fig. 11 has roughly a period of 100 ns, which corresponds to a frequency of 10 MHz and a $\omega\tau_s$ of ~ 0.26. This $\omega\tau_s$ would correspond to an increase in amplitude of just over 3% for a purely sinusoidal wave, which is significantly less than what we observed. However, the signal is not sinusoidal and has Fourier components well above 10 MHz and some above 38 MHz ($\omega\tau_s \sim 1$). The combined amplification of all these components, even though most have $\omega\tau_s < 1$, causes an overall increase in the computed magnetic field when the self-induction term is included.

V. SUMMARY

The three-axis magnetic probe design, construction method, and calibration technique presented yield a viable diagnostic for studying fast (50 MHz) transient plasma phenomena in the laboratory setting. It is also shown that the first order correction, the $O(\omega)$ self-induction term, can have a non-negligible effect on the calculation of the magnetic field even when its magnitude is much less than that of the zeroth order term. This is due to the combined effect of the amplification over all of Fourier space. The probe behavior

in this respect is highly dependent on how the probe is designed and constructed. Some probes used in the past had larger self-inductances and capacitances than the one presented here. As a result, their frequency responses deviated greatly from the ones presented in this paper.

The 14-bit, 100 MHz DAQ system used to acquire the signal in Fig. 11 was able to resolve and digitize the signal, but the temporal resolution is coarse. In the 80 μs it took for the edge of the bubble to pass the probe tip, only eight data points were taken. As a result, the signals were under sampled causing the peak signal to be under resolved and likely causing the magnetic field to be underestimated. A faster DAQ system is required to improve the temporal resolution.

Future studies are planned to further improve on the probe design, calibration, and analysis. Efforts will be put into decreasing the probe's physical size to be smaller than the ion-Larmour radius and reducing stray pickup. An improved calibration setup is being developed to characterize the probe's frequency response above 50 MHz. Finally, a high-frequency integrating circuit will be developed to eliminate the error incurred from the discrete integration described in Sec. IV A.

ACKNOWLEDGMENTS

This work is supported by the Department of Energy (DOE) (Grant No. DE-FG02–06ER54906) and the National Science Foundation (NSF) (Grant No. NSF 05–619) partnership in Basic Plasma Science, the Basic Plasma Science Facility at the University of California, Los Angeles (UCLA), and the NSF REU program. We would like to thank W. Gekelman and T. Carter for fruitful discussions on the probe theory and analysis, M. Nakamoto and Z. Lucky for helpful suggestions on probe design and construction, and S. Vincena, A. Collette, and S. Tripathi for their assistance with the experiment on the LAPD.

[1] W. Gekelman, A. Collette, and S. Vincena, Phys. Plasmas **14**, 062109 (2007).
[2] B. H. Ripin, J. D. Huba, E. A. Mclean, C. K. Manka, T. Peyser, H. R. Burris, and J. Grun, Phys. Fluids B **5**, 3491 (1993).
[3] V. P. Bashurin, A. I. Golubev, and V. A. Terekhin, J. Appl. Mech. Tech. Phys. **24**, 614 (1983).
[4] Y. P. Zakharov, IEEE Trans. Plasma Sci. **31**, 1243 (2003).
[5] T. A. Carter, B. Brugman, P. Pribyl, and W. Lybarger, Phys. Rev. Lett. **96**, 155001 (2006).
[6] A. Nawaz, M. Lau, G. Herdrich, and M. Auweter-Kurtz, AIAA J. **46**, 2881 (2008).
[7] H. Koizumi, R. Noji, K. Komurasaki, and Y. Arakawa, Phys. Plasmas **14**, 033506 (2007).
[8] P. Y. Peterson, A. D. Gallimore, and J. M. Haas, Phys. Plasmas **9**, 4354 (2002).
[9] S. Vincena, W. Gekelman, and J. Maggs, Phys. Plasmas **8**, 3884 (2001).
[10] I. H. Hutchinson, *Principles of Plasma Diagnostics* (Cambridge University Press, United Kingdom, 1987), pp. 10–14.
[11] P. A. Miller, E. V. Barnat, G. A. Hebner, A. M. Paterson, and J. P. Holland, Plasma Sources Sci. Technol. **15**, 889 (2006).
[12] J. Spaleta, L. Zakharov, R. Kaita, R. Majeski, and T. Gray, Rev. Sci. Instrum. **77**, 10E305 (2006).
[13] R. S. Shaw, J. H. Booske, and M. J. McCarrick, Rev. Sci. Instrum. **58**, 1204 (1987).
[14] R. C. Phillips and E. B. Turner, Rev. Sci. Instrum. **36**, 1822 (1965).
[15] J. G. Yang, J. H. Choi, B. C. Kim, N. S. Yoon, and S. M. Hwang, Rev. Sci. Instrum. **70**, 3774 (1999).
[16] S. Messer, D. D. Blackwell, W. E. Amatucci, and D. N. Walker, Rev. Sci. Instrum. **77**, 115104 (2006).
[17] M. P. Reilly, W. Lewis, and G. H. Miley, Rev. Sci. Instrum. **80**, 053508 (2009).
[18] C. Constantin, W. Gekelman, P. Pribyl, E. Everson, D. Schaeffer, N. Kugland, R. Presura, S. Neff, C. Plechaty, S. Vincena, A. Collette, S. Tripathi, M. Villagran Muniz, and C. Niemann, Astrophys. Space Sci. **322**, 155 (2009).
[19] W. Gekelman, H. Pfister, Z. Lucky, J. Bamber, D. Leneman, and J. Maggs, Rev. Sci. Instrum. **62**, 2875 (1991).
[20] W. Gekelman, M. VanZeeland, S. Vincena, and P. Pribyl, J. Geophys. Res. **108**, 1281 (2003).
[21] M. VanZeeland and W. Gekelman, Phys. Plasmas **11**, 320 (2004).
[22] S. Kacenjar, M. Hausman, M. Keskinen, A. W. Ali, J. Grun, C. K. Manka, E. A. McLean, and B. H. Ripin, Phys. Fluids **29**, 2007 (1986).